Radio Interferometry Measurements of a 16-km Baseline With 4-cm Precision

J. B. Thomas, J. L. Fanselow, and P. F. MacDoran
Tracking and Orbit Determination Section

D. J. Spitzmesser
Network Operations Office

L. Skjerve
Philco-Ford Corporation
Barstow, California

In order to demonstrate the feasibility of eventually using radio interferometry techniques to measure tectonic motion, a series of interferometry experiments has been conducted between two antennas at the Goldstone Deep Space Communications Complex. The primary objective of these experiments was to develop independent-station instrumentation capable of making three-dimensional baseline measurements with an accuracy of a few centimeters. To meet this objective, phase-stable instrumentation was developed to precisely measure the time delay by means of two-channel bandwidth synthesis. Delay measurements produced by this instrumentation lead to three-dimensional baseline measurements with a precision of 2–5 cm for the components of a 16-km baseline.

I. Introduction

In the last few years, there has been increasing interest in developing a system capable of accurately measuring the relative motion of points separated by distances ranging from 100 km up to intercontinental distances on the Earth's crust. Information concerning this far-field motion is of critical importance in the development of theoretical models of crustal dynamics. Since crustal motion is about 3–10 cm/year, the measurement accuracy should be about 1–3 cm with about 1 week of data. Radio interferometry is one technique that holds great promise for fulfilling this accuracy requirement.

In order to begin development of a radio system with few-centimeter accuracy, a series of interferometry experiments has been conducted between two antennas at the Goldstone Deep Space Communications Complex. The primary objective of these experiments was to develop independent-station instrumentation capable of making three-dimensional baseline measurements with an accuracy of a few centimeters. A short Goldstone baseline (16 km between DSS 12 and DSS 14) was selected so that transmission media uncertainties and astronomical parameters would be relatively unimportant compared with

radio system limitations. These experiments led to the refinement of a two-channel approach to bandwidth synthesis, a technique for measuring time delay that was originally developed by A. E. E. Rogers (Ref. 1). In this report, the instrumentation, analysis, and results of these Goldstone experiments are presented.

II. Radio Interferometer Technique

In the radio interferometry measurements described in this report, two antennas simultaneously receive the radio noise generated by an extragalactic radio source, as shown in Fig. 1. Because of a difference in ray paths, a given wave front will reach the two antennas at different times. This difference in arrival times is called the time delay τ. In this section, the technique for the measurement of this delay is described, while a mathematical model for this quantity is discussed in Section IV.

Since the radio interferometry method has been analyzed in detail in other papers (Refs. 1–6), it will be described only briefly in this report. Single-channel interferometry will be reviewed first, followed by an outline of two-channel bandwidth synthesis.

In single-channel measurements, each antenna system records on magnetic tape radio noise centered at frequency ω_a with bandwidth W_B. The tapes are then carried to a central site for digital processing. In this reduction, the two data streams are processed to obtain the stopped fringes (Ref. 5), which, for channel a, are given by

$$U_a(t, \tau_m) = A_B \frac{\sin(\pi W_B \Delta\tau_r)}{\pi W_B \Delta\tau_r} \cos\phi_s \qquad (1)$$

where the stopped phase is given by

$$\phi_s = \epsilon t + \omega_a(\tau_g + \tau_t + \tau_I - \tau_m) + \psi_a + C_a + R_a$$

In addition,

$$\Delta\tau_r = \tau_g + \tau_t + \tau_I + \tau_c - \tau_m \qquad (2)$$

In these expressions,

W_B = single-channel bandwidth

ω_a = effective interferometer bandpass center

ψ_a = instrumental phase drifts

C_a = differential charged-particle phase shift

R_a = brightness transform phase

τ_g = geometric delay

τ_t = differential tropospheric delay

τ_c = differential ionospheric delay

τ_I = instrumental delays plus clock synchronization error

τ_m = model delay

ϵ = analytical frequency offset

A_B = peak amplitude

Thus the stopped fringes are a product of an amplitude factor A_B, a delay curve, $\sin(\pi W_B \Delta\tau_r)/(\pi W_B \Delta\tau_r)$, and a sinusoidal function, $\cos\phi_s$. The amplitude factor depends on the brightness transform in addition to signal and system noise temperatures. The delay curve is a measure of bit stream alignment in the time domain, including all group delay effects. This particular form for the delay curve assumes that the system bandpass is rectangular with a linear phase-versus-frequency response, an approximation of negligible error for the purposes of this experiment. Finally, ϕ_s describes the phase behavior of the system. In this phase is buried the geometric delay τ_g, the observable of primary interest in these measurements. Note that, since the ionosphere is a dispersive medium, the ionosphere effect has been expressed as a phase shift in the fringe phase and as a delay in the total group delay.

The next step in the data reduction is to determine the fringe phase ϕ_s by a process known as phase tracking (Ref. 5), a technique that fits a least-squares sinusoid to the stopped fringes U_a. After $\phi_s(t)$ is extracted as a function of time, the analytical offset ϵt is removed in a manner that gives the correct sign (Ref. 5) to the resulting residual phase. The theoretical behavior of this measured residual phase $\Delta\phi_a$ is given by

$$\Delta\phi_a = \omega_a(\tau_g + \tau_t + \tau_I - \tau_m) + \psi_a + C_a + R_a \qquad (3)$$

The adjective "residual" denotes the fact that, in effect, the data reduction process subtracts a model delay (τ_m) from the fringe phase. This "phase stopping" procedure removes most of the time-varying components of the total delay.

Because fringe phase can be determined only to within a constant ($2n\pi$), narrow-band, single-channel interferometry can essentially measure only phase changes. Therefore, if residual phase is measured over a short time interval, it is essentially a measure of residual fringe frequency given by

$$\Delta\nu_a \equiv \Delta\dot{\phi}_a = \omega_a(\dot{\tau}_g + \dot{\tau}_t + \dot{\tau}_I - \dot{\tau}_m) + \dot{\psi}_a + \dot{C}_a + \dot{R}_a \qquad (4)$$

where $\Delta\dot{\phi}_a$ is the time derivative of the phase extracted from the fringes. This time derivative is insensitive to the z-component of the baseline, since that particular projection does not change appreciably as the Earth rotates. Consequently, a measurement of delay is essential if three-dimensional baseline measurements are to be made. This requirement for delay measurements lead to the development of two-channel bandwidth synthesis.

In two-channel bandwidth synthesis, the output of each antenna system is alternately switched between two narrow-band channels. For example, during even seconds, both systems would record a bandpass centered at ω_a, while during odd seconds, both would record at ω_b. For channel ω_b, the stopped fringes and fringe phase expressions would be identical to Eq. (1) and Eq. (2), except that the subscript a is replaced by b. An example of two-channel stopped fringes (Eq. 1) with one-second switching is shown in Fig. 2. On this Goldstone baseline, this radio source, 3C 454.3, has a correlated flux strength of about 10 flux units (one flux unit = 10^{-26} W/m^2/Hz). The amplitude noise on the fringes comes primarily from system noise (receiver, source, and background noise). This plot, which exhibits the first 30 s from a 600-s tape-pair, displays fringe points containing 0.5 s of data recorded at a 48-kilobit/s rate. Alternate seconds in the plot switch between fringes from two channels centered at 2270 MHz and 2310 MHz. The stopped fringe frequency is about 0.1 Hz in both channels and is due primarily to an analytical rate offset ϵ in the phase model used in fringe stopping. This offset allows a determination of the sign (Ref. 5) of the residual fringe frequency $\Delta\nu_a$ and $\Delta\nu_b$ (Eq. 4).

Fringe phase plots obtained from these fringes are shown in Fig. 3. Each phase point contains 50 s of data (100 fringe points of the type in Fig. 2), while the entire plot covers a complete tape-pair (600 s). In the plot, the error bars on the phase points represent the phase error produced by the actual amplitude noise on the fringes. The slope of each of these phase plots is a measurement of residual fringe frequency represented analytically in Eq. (4). Since an accurate model delay was used in the data reduction, the phase slopes are relatively constant over one tape. The small nonlinear trends ($\approx$0.03 cycle = 0.4 cm) that are present could be due to ionospheric effects. (Nonlinear trends due to large *a priori* delay errors would be quadratic in appearance over this short time interval.) Fringe frequency values obtained from the phase slopes are important interferometer observables and are utilized as shown in Section V.

In addition to the frequency observable, the measured delay values can be obtained by combining the phase output of the two channels as follows:

$$\Delta\tau = \frac{\Delta\phi_a - \Delta\phi_b}{\omega_a - \omega_b} \tag{5}$$

This computed value will be referred to as the a priori residual delay. The use of the term "residual" means that a model delay has in effect been subtracted from the total delay, leaving a much smaller value. In combining the two phase outputs, care must be taken to avoid 2π ambiguities (Ref. 5). When computing $\Delta\tau$, one can assume that the channel separation $\omega_a - \omega_b$ is essentially exactly known, since frequency calibration is accurate to parts in 10^{12}.

An example of a delay calculation is shown in Fig. 4, where the phase values have been combined from Fig. 3. Note how the systematic phase trends in Fig. 3 have disappeared in the difference, which in effect has scaled phase variations at S-band down to much lower levels at 40 MHz, the synthesized bandwidth. A covariance analysis indicates that the observed noise on these delay values comes almost entirely from the amplitude noise on the fringes. Over one tape, the residual delay $\Delta\tau$ is essentially constant due to an accurate delay model τ_m. Therefore, these delay values are averaged to produce one delay measurement for each tape-pair. After averaging, the resulting delay values, one for each tape-pair, become the primary observables of the interferometer system.

Note that, if the phase error in $\Delta\phi_a$ and $\Delta\phi_b$ is independent of frequency, the delay precision improves as the channel separation, $\omega_a - \omega_b$, increases. For this reason, the observing frequencies are generally separated as far as possible. As discussed in Section III, the maximum channel separation is determined by the bandpass limits of the antenna system.

The theoretical behavior of the measured delay is given by the expression (Ref. 5)

$$\Delta\tau = \Delta\tau_r + \frac{\psi_a - \psi_b}{\omega_a - \omega_b} = \tau_g + \tau_I + \tau_t + \tau_c - \tau_m + \frac{\psi_a - \psi_b}{\omega_a - \omega_b} \tag{6}$$

In the present measurements, the instrumental phase difference $\psi_a - \psi_b$ introduces a long-term linear drift in the measured delays. This drift is due primarily to a frequency offset between the frequency standards at the two stations. This term, as well as the other components of the measured delay, will be modeled in Section IV.

In summary, the data on each tape-pair are reduced to two observable values—time delay and fringe frequency.

Before proceeding to a discussion of the mathematical model for delay and the fitting procedure, the experiments and their instrumentation will be described.

III. Experiment Description

Over the last two years, five separate radio interferometry experiments, which are summarized in Table 1, have been conducted between DSS 12 and DSS 14 at the Goldstone Deep Space Communications Complex. All experiments involved S-band observations, JPL H-maser frequency standards, and a 24-kHz bandwidth digital recording system developed by D. S. Robertson and A. H. Legg of the Weapons Research Establishment, Australia. As indicated in Table 1, the various experiments were between 7 and 14 hours in duration and involved 13 to 18 radio sources. The sources used in the last four experiments are described in Table 2.

In the first Goldstone experiment (Ref. 2), one narrowband (24-kHz bandwidth) channel of radio noise was recorded, so that only the fringe frequency observable was precisely obtained. An analysis of the resulting frequency observables revealed frequency instability at the 1-mHz level ($\Delta f/f \approx 5 \times 10^{-13}$) over several hours. As indicated in Ref. 2, the HP5100 synthesizers associated with the first local oscillator (LO) signal were the most likely source of this instability. Consequently, in subsequent experiments, the synthesizers were replaced by more stable X7 multipliers, which will be described below.

After this first experiment, instrumentation was also developed to measure time delay in addition to fringe frequency. The technique adopted for delay measurements required the measurement of more than one channel of radio noise. This technique, commonly called bandwidth synthesis (Refs. 1 and 5), combines, either directly or indirectly, the fringe phase information of band-limited channels recorded at frequencies whose separations are large compared to that of the single-channel bandwidth.

In the original application of the bandwidth synthesis technique (Ref. 1), six channels were recorded in a time-shared mode. However, because of signal-to-noise ratio (SNR) improvement and simplification of instrumentation, we employed instrumentation that recorded only two channels. The only disadvantage of the two-channel system is that sufficiently precise *a priori* delay information is required to avoid 2π ambiguities (Ref. 5). Since delay measurement precision improves as channel separation increases, the goal of the instrumental design was to obtain maximum channel separation within the restrictions of the DSN antenna systems. In the final system, the maximum separation was defined by the limits of the traveling wave maser (TWM) receiver bandpass.

For the second experiment, a relatively simple instrumental configuration was devised to demonstrate the feasibility of the two-channel approach to bandwidth synthesis. In this intermediate system, which will not be described here in detail, two channels separated by 10 MHz at S-band were heterodyned to intermediate frequency (IF) and added. This combined signal was then heterodyned to baseband and continuously sampled at a 48-kilobit/s rate. While this system pays a price in SNR, it avoids the complications of simultaneous recorder channel switching at the two stations. This intermediate instrumentation demonstrated the feasibility of the two-channel approach and helped perfect the final instrumentation described below.

The final configuration used for bandwidth synthesis is shown in Fig. 5. In this system, a 10-MHz signal from the H-maser is converted to a 2240-MHz first LO signal by using only multipliers—the standard X4X8 multipliers of the DSN system and a new X7 multiplier. This X7 multiplier, which was constructed[1] to avoid the use of a synthesizer, converts the input sinusoid to a square wave, then filters and amplifies the seventh harmonic.

In order to achieve maximum channel separation and better delay precision, the S-band traveling wave maser receiver bandpass was broadened by retuning the trim coil currents. In this retuned state, the receiver exhibited ample amplification over a 40-MHz interval (2270 to 2310 MHz) while maintaining an operating system noise temperature less than 30 K. Therefore, after mixing with the first LO signal at 2240 MHz, the edges of the receiver passband were placed at 30 MHz and 70 MHz. However, this frequency spread exceeded the bandpass of the standard first mixer/preamplifier, which possesses adequate gain only over 45 to 55 MHz. Consequently, the standard mixer/preamplifier was replaced by a similar module with a bandpass between 10 and 160 MHz, thereby making the system TWM-limited. This IF passband was then filtered into two channels—one centered at 30 MHz and the other at 70 MHz. Each channel was mixed with a 20-MHz signal derived from the H-maser and each mixer response was appropriately filtered to place both channels at 50 MHz. At this point, each channel was transferred on alternate seconds to the video converter. The video converter mixed the input IF signal to baseband with a 50-MHz signal derived from the H-maser. The resulting time-shared

[1]R. L. Sydnor, Telecommunication Research Section, JPL.

baseband signal was then passed through a 24-kHz bandpass filter before digital sampling and recording at a 48-kilobit/s rate.

IV. Time Delay Model

The residual delay $\Delta\tau$ observed in radio interferometry measurements is a sum of geometric, instrumental, and transmission media delays, as indicated in Eq. (6). This section outlines the model adopted for these terms in the observed delay, starting with the largest and most important term, the geometric delay.

As indicated in Fig. 1, a given wave front will reach the two antennas of the interferometer at different times. It is readily shown that the geometric delay is given by the expression (Ref. 3)

$$\tau_g = -\frac{\mathbf{B}\cdot\hat{\mathbf{S}}}{c}\left(1+\frac{\mathbf{V}_2\cdot\hat{\mathbf{S}}}{c}\right) \tag{7}$$

where $\mathbf{B}$ is the baseline vector between the two antennas, $\mathbf{S}$ is the apparent source direction, $\mathbf{V}_2$ is the velocity of antenna 2, and c is the speed of light. Note that the geometric delay is essentially the instantaneous geometric path difference multiplied by a small correction that accounts for the motion of antenna 2 during the wave transit.

In the present analysis, true equatorial coordinates of date (TECD) are chosen as the coordinate frame for geometric delay calculations. In this Earth-centered right-handed frame, the z-axis is along the instantaneous spin axis of Earth while the x-axis is along the true equinox of date. The source vector $\mathbf{B}$ and the baseline vector $\hat{\mathbf{S}}$ can be expressed in terms of these coordinates as follows.

In TECD, the source vector $\mathbf{S}$ is usually characterized by two angles—apparent declinations δ_s and apparent right ascension α_s. These angles lead to the usual expression for the source vector:

$$\hat{\mathbf{S}} = (\cos\delta_s\cos\alpha_s, \cos\delta_s\sin\alpha_s, \sin\delta_s) \tag{8}$$

The term "apparent" indicates the presence of a correction to the source direction that accounts for aberration due to the Earth's orbital motion (Refs. 3 and 7). In addition, precession and nutation of the Earth's spin axis (Refs. 7 and 8) are included to rotate to TECD from mean equatorial coordinates of 1950.0 since the 1950.0 frame is conventionally used to catalogue source positions. In the present short-baseline measurements, these corrections are easily made with adequate accuracy.

The baseline vector $\mathbf{B}$ must include two general features: an Earth-fixed definition and Earth orientation factors. The Earth-fixed vector, $\mathbf{B}_{03}$, is defined in terms of a right-handed coordinate frame with a z-axis toward the Conventional International Origin (CIO) pole and X-axis along the Greenwich meridian. It will be represented in Cartesian coordinates as follows:

$$\mathbf{B}_{03} = (x_b, y_b, z_b) \tag{9}$$

where x_b, y_b are the equatorial components and z_b is the z-component, as schematically indicated in Fig. 1.

At this point in the discussion of the baseline vector, a definition of antenna location is desirable. The effective location of an antenna depends on antenna structure. Most directional antennas have two primary axes of rotation that allow antenna orientation. For DSS 14, an azimuth/elevation antenna, the rotation axes intersect. By geometrical considerations, one can show that this point of intersection is the effective antenna location.

On the other hand, DSS 12 is a polar mount, for which the rotation axes are nonintersecting. In this case, the effective location is the point at which the hour-angle axis orthogonally intersects a plane containing the declination axis. Therefore, for this polar mount, one must include the correction factor $b\cos\delta_s$ in delay calculations, where b is the shortest distance between the two axes. This correction factor accounts for the fact that this type of antenna "stretches toward" low-declination objects. For DSS 12, the axis separation b is 6.706 m and is easily accounted for with adequate precision.

The baseline vector $\mathbf{B}$ rotates in space as a result of polar motion and Earth spin. To account for those motions, the Earth-fixed baseline vector is rotated to its instantaneous orientation in TECD as follows:

$$\mathbf{B}(t) = R_e R_p \mathbf{B}_{03} \tag{10}$$

where the Earth spin matrix is given by the expression

$$R_e = \begin{pmatrix} \cos\alpha_G & -\sin\alpha_G & 0 \\ \sin\alpha_G & \cos\alpha_G & 0 \\ 0 & 0 & 1 \end{pmatrix} \tag{11}$$

and the polar motion matrix is given by

$$R_p = \begin{pmatrix} 1 & 0 & -X_p/a \\ 0 & 1 & Y_p/a \\ X_p/a & -Y_p/a & 1 \end{pmatrix} \tag{12}$$

In these expressions, the angle α_G is the hour angle of the equinox at the time of interest and is easily obtained from universal time (UT1). Parameters X_p and Y_p are the polar displacements relative to the CIO pole, while a is the polar radius. See Ref. 3 for more detail concerning these Earth orientation factors.

The expressions above for **B** and $\hat{\mathbf{S}}$ are easily combined to calculate the geometric delay for a given source. It should be noted that the model for the geometric delay outlined above neglects general relativistic effects which, for longer baselines, may be significant.

In these experiments, no corrections were made for ionospheric effects. In all the measurements reported here, radio sources were observed at night when ionospheric delays, inhomogeneities, and turbulence were at a minimum. At S-band, the nighttime ionosphere causes about a 1-m delay along a single ray path at a typical elevation angle ($\approx$30 deg). However, the *difference* in ionospheric delays along the two interferometer ray paths is the important quantity in delay measurements. Since nighttime observations involve a relatively homogeneous ionosphere, this difference for a 16-km baseline will be a small fraction of a single ray-path delay. As we shall see, the delay residuals in the present experiments strongly indicate that differential ionosphere delays were less than 6 cm. Below the 6-cm level, differential ionosphere corrections, even if they were available, would be of marginal value in the present delay measurements. However, as discussed in Section VI, the frequency residuals contain an unmodeled noise term at the 0.1-mHz level that could possibly be an ionospheric effect.

The total troposphere delay for a single ray path is about 4 m for a typical elevation angle. In the present work, small corrections are made to the delay observables to remove small known differences ($\leq$15 cm) in tropospheric delays along the two ray paths. These differences are a consequence of Earth curvature as well as a slight altitude difference (40 m) between the two antennas. The altitude difference produces a 1-cm difference in the "dry" component of the zenith tropospheric delay. The Earth's curvature leads to elevation angle differences that cause differential troposphere corrections as large as 10 cm. It is believed that, with these corrections, the differential "dry" troposphere delay becomes a negligible source of error. The total "wet" troposphere delay for one ray path at Goldstone is only 10–20 centimeters at typical elevation angles. For a 16-km baseline with only small changes in altitude, the difference in the wet troposphere between ray paths should be only a small fraction ($<$10%) of the single ray path delay. It is estimated that, with the listed corrections, the total troposphere effect in the delay observable becomes a negligible source of error ($\leq$3 cm).

Finally, with regard to the present instrumentation, the instrumental terms (τ_I, $\psi_a - \psi_b$) in the measured delay (Eq. 6) can be adequately modeled as a constant plus a linear drift, where the constant and slope are used as solve-for parameters.

V. Fitting Procedure

As outlined in Section II, the reduction of each tape-pair gives the residual delay $\Delta\tau$ and fringe frequency $\Delta\nu$ for a particular radio source observed for a 12-min interval. In order to extract the baseline vector, the delay and frequency values from many tape-pairs recorded for many radio sources must be simultaneously fit by a least-squares technique using a model for the delay. The construction of a mathematical model for the geometric delay was outlined in Section IV. This section outlines the weighted least-squares fitting procedure used to extract the Goldstone baseline.

In these short-baseline measurements, uncertainties in the geometric delay due to errors in source location and Earth orientation factors (polar motion, UT1, precession, nutation) are small compared with instrumental errors. That is, all of these factors have been measured with sufficient accuracy by other methods so that they may be treated as "known" quantities in delay calculations. For the radio sources in these experiments, source locations have been independently measured with an accuracy of 0.2–0.9 arc seconds, as indicated in Table 2. The position errors in this table represent approximate external accuracy, conservatively estimated in some cases by root-sum-squaring the quoted internal errors with 0.3 arc second. The adequacy of these measurements can be demonstrated by the following approximate calculation. A typical value for the sensitivity partials in the present experiments is approximately 0.1 ns/arc second. When this sensitivity is multiplied by a typical source location error of about 0.5 arc second, a delay error equal to 0.05 ns (1.5 cm) results. This delay error is small compared with a typical system noise error of about 7 cm. Similar detailed calculations for all sources in Table 2 indicate that these source positions are adequate for present delay model calculations. By similar arguments, one can show that polar motion and UT1, which are known with about 0.03 arc second accuracy (Ref. 9), also contribute negligible errors in delay calculations. The BIH values for UT1 − UTC and polar motion parameters are listed in Table 3. Finally,

known errors in the models for precession and nutation of the Earth's spin axis contribute errors less than 0.2 arc second (Ref. 8), and may be regarded as negligible. Therefore, only the three baseline parameters must be regarded as solve-for parameters in the geometric delay.

In addition to the geometric delay parameters, the observed delay contains unknown offset and linear drift terms which are equivalent in effect to a synchronization error and rate difference between clocks. The linear drift is due mainly to a small uncalibrated rate difference between the H-maser frequency standards. In the fringe frequency observable, the rate difference becomes a constant frequency offset. In principle, the frequency offset and the delay rate offset should be equal. However, as will be shown, the fringe frequency observable contains extra noise considerably above the expected system noise. In addition, the frequency observable contains elements of the frequency system that cancel in the delay observable. For these reasons, the two rate factors are varied independently in the fit so that the frequency offset can freely seek its own level without coupling in a corrupting fashion with the delay observable. However, comparison of the two rate offsets is one means of judging the quality of these measurements.

Under these assumptions, the complete models[2] for the residual delay and fringe frequency observables become

$$\Delta\tau_i = \left.\frac{\partial\tau_g}{\partial x_b}\right|_i \Delta x_b + \left.\frac{\partial\tau_g}{\partial y_b}\right|_i \Delta y_b + \left.\frac{\partial\tau_g}{\partial z_b}\right|_i \Delta z_b + \tau_s + \dot{\tau}_s t_i \tag{13}$$

$$\Delta\nu_i = \left.\frac{\partial\nu_g}{\partial x_b}\right|_i \Delta x_b + \left.\frac{\partial\nu_g}{\partial y_b}\right|_i \Delta y_b + \nu_s \qquad i = 1, N_t \tag{14}$$

where $\Delta\tau_i, \Delta\nu_i$ are the *a priori* residual delay and fringe frequency for the ith tape-pair recorded at time t_i, and N_t is the total number of tape-pairs.

The terms in Eqs. (13) and (14) have been accounted for as follows. The first terms with partials are the usual linear expansions of the residual geometric delay, $\tau_g - \tau_m$, where Δx_b, Δy_b, and Δz_b are the solve-for deviations from the three components of the *a priori* baseline used in τ_m. The delay terms τ_s and $\dot{\tau}_s$ account for the instrumental phase effects entering in the difference $\Delta\phi_a - \Delta\phi_b$. The parameter ν_s is the offset in the fringe frequency observable. As indicated in Section IV, transmission media delays are assumed to be a negligible source of error after small tropospheric corrections. Thus, there are six solve-for parameters in the fitting procedure: Δx_b, Δy_b, Δz_b, τ_s, $\dot{\tau}_s$, ν_s.

Extra frequency noise, which is discussed in Section VI, reduced the strength of the fringe frequency observables. Normally, if only system noise is present, each channel contributes a statistically independent measure of fringe frequency. The extra frequency noise in the present experiment was almost perfectly correlated between channels. This correlation meant, in effect, that the two channels produced only one independent fringe frequency measurement for each tape-pair.

In order to simultaneously fit the delay and frequency observables, the fitting equations (Eq. 13 and 14) are more conveniently expressed in the following form:

$$u = Ap \tag{15}$$

where

$$u = \begin{pmatrix} \Delta\tau_1 \\ \Delta\tau_2 \\ \cdot \\ \cdot \\ \cdot \\ \Delta\tau_{N_t} \\ \Delta\nu_1 \\ \cdot \\ \cdot \\ \cdot \\ \Delta\tau_{N_t} \end{pmatrix} \qquad p = \begin{pmatrix} \Delta x_b \\ \Delta y_b \\ \Delta z_b \\ \tau_s \\ \dot{\tau}_s \\ \nu_s \end{pmatrix} \tag{16}$$

and

$$A = \begin{pmatrix} \left.\frac{\partial\tau_g}{\partial x_b}\right|_1 & \left.\frac{\partial\tau_g}{\partial y_b}\right|_1 & \left.\frac{\partial\tau_g}{\partial z_b}\right|_1 & 1 & t_1 & 0 \\ \left.\frac{\partial\tau_g}{\partial x_b}\right|_2 & \left.\frac{\partial\tau_g}{\partial y_b}\right|_2 & \left.\frac{\partial\tau_g}{\partial z_b}\right|_2 & 1 & t_2 & 0 \\ \cdot & \cdot & \cdot & \cdot & \cdot & \cdot \\ \cdot & \cdot & \cdot & \cdot & \cdot & \cdot \\ \cdot & \cdot & \cdot & \cdot & \cdot & \cdot \\ \left.\frac{\partial\tau_g}{\partial x_b}\right|_{N_t} & \left.\frac{\partial\tau_g}{\partial y_b}\right|_{N_t} & \left.\frac{\partial\tau_g}{\partial z_b}\right|_{N_t} & 1 & t_{N_t} & 0 \\ \left.\frac{\partial\nu_g}{\partial x_b}\right|_1 & \left.\frac{\partial\nu_g}{\partial y_b}\right|_1 & 0 & 0 & 0 & 1 \\ \cdot & \cdot & \cdot & \cdot & \cdot & \cdot \\ \cdot & \cdot & \cdot & \cdot & \cdot & \cdot \\ \cdot & \cdot & \cdot & \cdot & \cdot & \cdot \\ \left.\frac{\partial\nu_g}{\partial x_b}\right|_{N_t} & \left.\frac{\partial\nu_g}{\partial y_b}\right|_{N_t} & 0 & 0 & 0 & 1 \end{pmatrix} \tag{17}$$

[2]The geometric fringe frequency is defined by $\nu_g \equiv \omega_a \dot{\tau}_g$.

The weighted least-squares solution for p is given by the standard matrix expression (Ref. 10)

$$\hat{p} = (A^T W A)^{-1} A^T W u \tag{18}$$

where the diagonal weighting matrix W is given by

$$W = \begin{pmatrix} \frac{1}{\sigma^2_{\tau_1}} & & & & 0 \\ & \frac{1}{\sigma^2_{\tau_2}} & & & \\ & & \ddots & & \\ & & & \frac{1}{\sigma^2_{\tau_{N_t}}} & \\ & & & & \frac{1}{\sigma^2_{v_1}} \\ & & & & & \ddots \\ 0 & & & & & & \frac{1}{\sigma^2_{v_{N_t}}} \end{pmatrix} \tag{19}$$

In the absence of *a priori* information concerning the model parameters, the vector $\hat{\mathbf{p}}$ is the best estimate of the solve-for parameters. In the weighting matrix W, σ_{τ_i} and σ_{v_i} are the *total* measurement error (1σ) on each delay and frequency observable. In this solution, it is assumed that the noise on a given observable is uncorrelated with the noise on any other observable, so that the off-diagonal elements of W are zero. For the present experiments, this assumption can be partially justified as follows. Delay and frequency observables are uncorrelated since, as revealed by the fits, the dominant uncertainty in delay is system noise, while in the frequency observable, the dominant uncertainty is due to some unmodeled noise source, probably unpredictable ionospheric variations. The observables obtained from different tape-pairs are uncorrelated with regard to system noise. It is assumed that the unmodeled frequency noise is also uncorrelated between tape-pairs.

The *a priori* observable noise was assigned on the basis of instrumental factors: system noise temperature and frequency standard noise.

$$\sigma^2_{\tau_i} = \sigma^2_{\tau_i}(s) + \sigma^2_{\tau}(f) \tag{20}$$

$$\sigma^2_{v_i} = \sigma^2_{v_i}(s) + \sigma^2_{v}(f) \tag{21}$$

where s denotes system noise and f denotes frequency standard noise. The system noise contribution to each observable was calculated by a covariance analysis based on amplitude noise on the fringes. (The fringe signal-to-noise ratio in this experiment is determined primarily by the usual factors: system noise temperature, correlated flux, and bit count per fringe point.) The frequency standard noise terms were assigned the following values based on typical JPL hydrogen maser stability ($\Delta f/f \approx 10^{-14}$). In the frequency domain, expected H-maser frequency noise is about 23 μHz at S-band for 700-s integration times. In the time domain, the effective delay (phase) noise introduced by the oscillators is estimated to be about 0.08 ns for 8 h of data. This delay noise estimate is considerably below the standard estimate ($\Delta\tau_l \approx 10^{-14} \times 8$ h ≈ 0.3 ns) because of the least-squares fitting procedure. That is, the delay offset and linear drift parameters contained in the fit absorb most of the delay excursions due to H-maser instability.

After a given fit, the best estimate of the fit function is given by

$$\hat{u} = A\hat{p} \tag{22}$$

The fit residuals for this process are given by the difference between the observables and the fit function:

$$\Delta u \equiv u - \hat{u} \tag{23}$$

Before the final simultaneous fit to both delay and frequency observables, preliminary fits were made *independently* to each observable type. These preliminary fits were used to establish the actual noise level in each observable type and to check for consistency in the resulting baseline (equatorial component) solutions. In the *first* independent fit to a given observable type, the weighting errors were assigned the *a priori* values based on instrumental factors in Eqs. (20) and (21). On the basis of this first fit using instrumental error estimates, fit residuals can be calculated for the data type under investigation. The noise exhibited by these residuals can be tested for conformity with the *a priori* error estimates by means of chi-square analysis. The fit chi-square is calculated according to the standard expression

$$\chi^2_h = \frac{1}{N_f} \sum_{i=1}^{N_t} \frac{(h_i - \hat{h}_i)^2}{\sigma^2_{h_i}} \tag{24}$$

where h denotes either the delay or the frequency data type and σ_{h_i} is the *a priori* error in each observable. The quantity N_f is the number of degrees of freedom given by

$$N_f = N_t - N_p \tag{25}$$

where N_p is the number of solve-for parameters (N_p is 3 for frequency observables and 5 for delay). If the fitting assumptions are correct, it can be shown that the chi-square value will be given on the average by

$$< \chi_h^2 > = 1.0 \pm \frac{1}{(2N_f)^{1/2}} \tag{26}$$

If the preliminary chi-square, based on instrumental noise, falls considerably above this range ($> 2\sigma$), then either the observable model is inadequate or the observable noise is higher than expected.

In the present data reduction efforts, the preliminary chi-square for a given data-type did fall above the allowed range in certain cases. However, in those cases, the extra noise on the residuals appeared to be uniformly distributed with no trends or singularly bad points. Therefore, the total noise on that observable type was uniformly increased by adding an extra error term as follows:

$$\sigma_{\tau_i}^2 = \sigma_{\tau_i}^2(s) + \sigma_\tau^2(f) + N_\tau^2 \tag{27}$$

for delay observables and

$$\sigma_{\dot{\nu}_i}^2 = \sigma_{\dot{\nu}_i}^2(s) + \sigma_{\dot{\nu}}^2(f) + N_{\dot{\nu}}^2 \tag{28}$$

for frequency observables. The least-squares fit was then rerun for that data-type and the extra error term (N_τ or $N_{\dot{\nu}}$) was adjusted to make chi-square equal to 1.0. Formally, this procedure assumes that the total observable noise contains, in addition to the expected instrumental noise, an extra noise source that affects all tape-pairs equally without correlations between tape-pairs. The principal argument in favor of this error adjustment procedure is that it is the simplest reasonable assumption that one can make when confronted with large, uniformly random residuals due to an unmodeled noise source. Furthermore, since large uniform residuals indicate degradation of the solution, this procedure, in a gross sense, accounts for this degradation in the fit and in the resulting covariance analysis for parameter errors.

After the observable noise was determined independently for each observable type by means of the chi-square analysis outlined above, the resulting observable weighting errors were used in a *simultaneous* fit to the delay and frequency observables to determine the baseline. This procedure was repeated for each experiment in Table 1, producing one baseline measurement per experiment.

After the final simultaneous fit, including error adjustments, the covariance error for the solve-for parameters was calculated by the standard expression (Ref. 10)

$$(\sigma_p)_k^2 = (A^T W A)_{kk}^{-1} \qquad k = 1, N_p \tag{29}$$

where

$$\sigma_p = (\sigma_{x_b}, \sigma_{y_b}, \sigma_{z_b}, \sigma_{\tau_s}, \sigma_{\dot{\tau}_s}, \sigma_{\nu_s})$$

These covariance error values will be referred to as the formal precision.

VI. Results and Discussion

The Goldstone baseline has been measured in five separate experiments by means of radio interferometry. The first of these experiments, in January, 1971, involved only fringe frequency measurements. Since that experiment has been described in a previous report (Ref. 2), only the resulting baseline value will be included here. This section will outline the fitting results for the four subsequent bandwidth synthesis experiments. The fits to the delay observable will be discussed first, followed by the fringe frequency results.

The delays observed in the first bandwidth synthesis experiment are shown in Fig. 6. This set of observations covered about 14 h and involved 15 separate radio sources. Each data point represents the delay value obtained from one 12-min tape-pair. These delays were measured using two 24-kHz channels separated by 10 MHz at S-band with H-maser frequency standards at each station. Note the delay offset and the linear drift that has been introduced by the instrumentation. The scatter in these delay values is due to an intentional 4-m bias in the *a priori* baseline that maps into a delay error which changes as the antennas move from source to source. After a least-squares fit for the baseline vector, delay offset, and delay rate, the delay values in Fig. 6 produce the reduced residuals in Fig. 7. Note that these residuals exhibit a fairly uniform scatter and an RMS spread of 4.7 ns.

Delay values measured in the second experiment (8/16/72) are shown in Fig. 8. In this case, the two 24-kHz channels were separated by 40 MHz, as discussed in Section III. This set of observations covered about 8 h and

involved 15 separate radio sources. Again, the scatter in delay values is due to an intentional error in the *a priori* baseline. After the least-squares fit, this wide scatter is reduced to the small delay residuals in Fig. 9 with an RMS spread of 0.5 ns. By contrasting these residuals with the residuals of the 10-MHz system in Fig. 7, one readily sees the improved precision of the larger synthesized bandwidth (note the scale change).

For the 40-MHz system, delay noise due to system noise temperature was 0.1–1.0 ns for correlated source strengths between 1 and 10 flux units. H-maser flicker noise ($\Delta f/f \approx 10^{-14}$) should contribute negligible delay noise ($\approx$0.08 ns) for 8-h fit intervals. In the fit to the delay observables in the first 40-MHz experiment (Fig. 9), an additional noise term N_τ equal to 0.25 ns had to be included to bring the delay chi-square value down to its proper range (see Section V for a discussion of observable noise adjustment). Because of this extra noise, the instrumentation configuration was checked for possible noise sources. In that configuration, the upper channel was on the wing of the system bandpass, down 30 dB from the bandpass center. In order to eliminate the possibility of differential phase instability due to this situation, the system bandpass was broadened by removing the S-band preselector in the DSIF receiver and by adjusting the maser magnetic field for the last two experiments. When the delay data were analyzed for these two reconfigured experiments, no extra delay noise was required to place the delay chi-square in its proper range. This fitting result is readily ascertained graphically by noting that the delay residuals for the last two experiments, Figs. 10 and 11, are less noisy than the residuals in Fig. 9. An upper limit on possible unmodeled noise sources can be established by increasing the noise term N_τ to the level that causes χ^2_τ to fall below 1.0 by 2σ. For the last two experiments, the value of N_τ required for such a χ^2 reduction is 6 cm. This result indicates that no unexpected (e.g., noninstrumental) noise sources greater than 6 cm were present in the delay observable.

The fact that the delay residuals were at the system noise limit places an upper bound on the differential ionosphere delays since the ionosphere effect should exhibit a fairly random sign and magnitude. That is, as the antennas move from source to source, the interferometer ray paths pierce areas of the ionosphere hundreds of kilometers apart. Since one would expect localized spatial inhomogeneities ($\leq$16 km) to be dissimilar over such a wide range, the differential ionosphere delays are probably fairly random and appear as delay noise. Therefore, because the delay residuals place a limit on additional noise, the differential ionosphere delays were evidently less than 6 cm.

In the fringe frequency fits, the residuals exhibited a random distribution with an rms spread of 0.1–0.2 mHz. An example of the frequency residuals is shown in Fig. 12. In all experiments the noise observed in the frequency residuals was considerably above the expected instrumental noise. For example, the expected instrumental frequency noise due to system noise temperature is 20–60 μHz for correlated source strengths between 3 and 10 flux units. In addition, H-maser flicker noise can contribute an uncertainty of about 25 μHz. However, for the last four experiments, the fitting procedure outlined in Section V required an additional noise term N_ν equal to 0.1–0.2 MHz to bring the frequency chi-square down to its proper range. The origin of this extra noise could easily be the ionosphere. For example, if the differential ionospheric delay changed by 1 cm in 700 s (one tape-pair), the frequency effect would be 0.15 mHz at S-band. Since the ionosphere delay for a single ray path is 1 m, differential delay changes of this magnitude (1%) seem reasonable.

The baseline components produced by all five experiments are shown in Table 4 and in Figs. 13 and 14. Note that as the frequency system stability improved and as bandwidth synthesis was introduced, the formal precision in the equatorial components steadily improved from 30 cm to about 3–5 cm. For the z-component, the improvement in measurement precision is even more dramatic. The first experiment (January, '72) did not determine the z-component, since only fringe frequency was measured. The second experiment (April, '72), with a 10-MHz synthesized bandwidth, measured the z-component with a formal precision of 45 cm. The last two experiments, utilizing a 40-MHz synthesized bandwidth, determined the z-component with a formal precision of about 3 cm. The three baseline components are easily combined to give the total length plotted in Fig. 14. Note that for all three components and the total length, all interferometry baseline measurements are in excellent agreement within the formal precision. This agreement indicates that the formal covariance errors described in Section V are accurate estimates of actual precision for the present system.

The baseline vector between DSS 12 and DSS 14 has also been determined by conventional survey techniques (Ref. 11) as indicated in Figs. 13 and 14 and in Table 4. Note that the *length* of the baseline vector obtained by geodetic traverse is in excellent agreement with the interferometry result. However, the results for the three components do not agree, particularly the z-component where the disagreement is about 60 cm (3σ). Both the interferometry and survey techniques are being investigated to determine the source of this disagreement.

VII. Summary and Conclusions

A series of Goldstone baseline (16-km) measurements have been conducted to demonstrate the feasibility of eventually using radio interferometry to monitor tectonic motion. In the course of these experiments, frequency- and phase-stable instrumentation was developed to allow delay measurements by means of two-channel bandwidth synthesis. The final system synthesized a 40-MHz bandwidth using a 24-kHz bandwidth digital recording system and H-maser frequency standards. The delay measurements produced by this system lead to precise three-dimensional baseline measurements. Because of instrumental improvements, the formal baseline precision improved from 30 cm to 4 cm with about 8 hours of data. In the last measurements, the delay residuals were found to lie at the system noise limit. This fact indicates that those delay observables were free of unmodeled noise above the 6-cm level. In addition, the three most precise baseline measurements were in excellent agreement within the expected statistics, which indicated a formal precision of 2–5 cm for the various components. This agreement strongly indicates that formal baseline errors produced by covariance analysis were good estimates of the actual precision of the present system.

Since instrumental precision is independent of baseline length, these Goldstone measurements demonstrate the feasibility of measuring baseline vectors of several thousand kilometers with ultimate accuracies of 1–4 cm. However, attainment of this accuracy for longer baselines will require additional calibrations for transmission media effects and whole-Earth motions such as universal time (UT1), polar motion, precession, and nutation.

Acknowledgments

The authors wish to acknowledge the contributions of C. J. Finnie, H. F. Fliegel, J. Gunckle, S. Petty, T. Sato, R. Sydnor, and J. G. Williams, of the JPL staff, and the personnel of the DSN Mars and Echo stations, particularly the servo, digital, and microwave subsystem operators.

References

1. Rogers, A. E. E., "Very Long Baseline Interferometry with Large Effective Bandwidth for Phase-delay Measurements," *Radio Science*, Vol. 5, No. 10, p. 1239, Oct. 1970.

2. Fanselow, J. L., et al., *The Goldstone Interferometer for Earth Physics*, Technical Report 32-1526, Vol. V, p. 45, Jet Propulsion Laboratory, Pasadena, Calif., Oct. 15, 1971.

3. Thomas, J. B., "An Analysis of Long Baseline Radio Interferometry," in *The Deep Space Network Progress Report*, Technical Report 32-1526, Vol. VII, p. 37, Jet Propulsion Laboratory, Pasadena, Calif., Feb. 1972.

4. Thomas, J. B., "An Analysis of Long Baseline Radio Interferometry, Part II," in *The Deep Space Network Progress Report*, Technical Report 32-1526, Vol. VIII, p. 29, Jet Propulsion Laboratory, Pasadena, Calif., May 1972.

References (contd)

5. Thomas, J. B., "An Analysis of Long Baseline Radio Interferometry, Part III," in *The Deep Space Network Progress Report*, Technical Report 32-1526, Vol. XVI, p. 47, Jet Propulsion Laboratory, Pasadena, Calif., Aug. 15, 1973.
6. Swenson, F. W., and Mathur, N. C., "The Interferometer in Radio Astronomy," *Proc. IEEE*, Vol. 56, p. 2114, 1968.
7. *Explanatory Supplement to the Ephemeris*, H. M. Stationery Office, London, 1961.
8. Melbourne, W. G., et al., *Constants and Related Information for Astrodynamic Calculations, 1968*, Technical Report 32-1306, Jet Propulsion Laboratory, Pasadena, Calif., July 1968.
9. *Notice to Users of Circular D*, Bureau International de l'Heure, Paris, March 2, 1971.
10. Solloway, C. B., *Elements of the Theory of Orbit Determination*, JPL Engineering Planning Document 255, Dec. 1964 (JPL internal document).
11. Meade, B. K., National Geodetic Survey, Rockville, Maryland, private communication for survey between Goldstone benchmarks at ECHO and MARS. W. Bollinger, JPL, private communication for surveys between DSS 12 and DSS 14 and their respective ground level benchmarks.
12. Kristian, J., and Sandage, A., *Astrophys. J.* 162, p. 391–398, 1970.
13. Fanselow, J. L., JPL, private communication.
14. Argue, A. N., and Kenworthy, C. M., *Nature*, Vol. 228, p. 1076, 1970.
15. Hunstead, R. W., *Mon. Not. R. Astr. Soc.*, Vol. 152, p. 227–294, 1971.
16. Adgie, R. L., Crowther, J. H., and Gent, H., *Mon. Not. R. Astr. Soc.*, Vol. 159, p. 233–251, 1972.
17. Hazard, C., et al., *Nat. Phys. Sci.*, Vol. 233, p. 89, 1971.
18. Veron, M. P., *Astron. and Astrophys.*, Vol. 20, p. 471–473, 1972.

Table 1. Summary of Goldstone interferometry experiments

Experiment	Synthesized bandwidth, MHz	Observation Period, h	No. of Tape-pairs	No. of Sources	Observables
A (71/1/29)	–	11	37	14	Frequency
B (72/4/4)	10	14	37	15	Frequency, delay
C (72/8/16)	40	8	25	15	Frequency, delay
D (72/10/14)	40	7	24	18	Frequency, delay
E (72/10/18)	40	7	19	13	Frequency, delay

Table 2. Sources used in Experiments B–E[a]

Source	Position (1950.0)		Approximate correlated flux (f.u.)	Observations[a] per experiment		Reference
	α_s	δ_s				
P 0106 + 01	1 6 4.48 ± 0.024	1 19 1.45 ± 0.3	1.7 — 2.5	B(1)	C(2)	
				D(1)	E(0)	12
DW 0224 + 67	2 24 41.14 ± 0.033	67 7 39.61 ± 0.5	1.1 — 1.7	B(0)	C(1)	
				D(2)	E(2)	13
P 0237 − 23	2 37 52.62 ± 0.033	−23 22 6.0 ± 0.32	4.5 — 5.5	B(0)	C(2)	
				D(3)	E(2)	12
3C 84	3 16 29.55 ± 0.02	41 19 52.2 ± 0.3	10 — 13	B(0)	C(1)	
				D(1)	E(2)	14
NRAO 190	4 40 5.27 ± 0.033	−0 23 20.0 ± 0.45	2.5 — 3	B(2)	C(0)	
				D(1)	E(2)	12
3C 138	5 18 16.525 ± 0.024	16 35 26.75 ± 0.36	5 — 6	B(0)	C(1)	
				D(1)	E(1)	12
P 0521 − 36	5 21 12.95 ± 0.028	−36 30 16.0 ± 0.68	2.5 — 3	B(0)	C(0)	
				D(1)	E(1)	15
P 0736 + 01	7 36 42.53 ± 0.028	1 43 59.9 ± 0.5	2	B(0)	C(0)	
				D(1)	E(0)	15
4C 55.16	8 31 4.38 ± 0.05	55 44 41.8 ± 0.4	8	B(3)	C(0)	
				D(1)	E(1)	16
P 0834 − 20	8 34 24.56 ± 0.04	−20 6 29.7 ± 0.45	2	B(3)	C(0)	
				D(1)	E(1)	12
P 1127 − 14	11 27 35.61 ± 0.033	−14 32 54.0 ± 0.45	3 — 5	B(4)	C(0)	
				D(0)	E(0)	12
3C 273	12 26 33.239 ± 0.013	2 19 43.28 ± 0.2	15 — 20	B(6)	C(0)	
				D(0)	E(0)	17
3C 309.1	14 58 56.70 ± 0.06	71 52 10.8 ± 0.32	3 — 3.5	B(4)	C(1)	
				D(0)	E(0)	12
3C 345	16 41 17.56 ± 0.033	39 54 10.7 ± 0.36	7 — 8	B(4)	C(2)	
				D(1)	E(0)	12
NRAO 530	17 30 13.43 ± 0.04	−13 2 46.2 ± 0.54	2.5 — 3	B(0)	C(1)	
				D(1)	E(0)	12
P 1741 − 038	17 41 20.61 ± 0.033	−3 48 49.2 ± 0.5	2.5 — 3	B(1)	C(1)	
				D(1)	E(0)	13
3C 371	18 7 18.49 ± 0.04	69 48 57.55 ± 0.36	1.5 — 2	B(2)	C(2)	
				D(1)	E(1)	12
P 2134 + 004	21 34 5.28 ± 0.033	0 28 25.9 ± 0.5	5.5 — 7	B(2)	C(1)	
				D(2)	E(1)	18
VRO 42.22.01	22 0 39.31 ± 0.04	42 2 9.0 ± 0.4	5.5 — 7	B(2)	C(3)	
				D(2)	E(3)	16
P 2203 − 18	22 3 25.675 ± 0.028	−18 50 16.8 ± 0.28	3.5 — 5	B(1)	C(4)	
				D(2)	E(1)	12
3C 454.3	22 51 29.485 ± 0.033	15 52 54.45 ± 0.45	10 — 11	B(1)	C(2)	
				D(1)	E(1)	12
P 2345 − 16	23 45 27.70 ± 0.028	−16 47 52.7 ± 0.42	2.5	B(1)	C(1)	
				D(0)	E(0)	15

[a]See Table 1.

Table 3. Time and polar motion parameters used in Experiments B–E

Experiment	UT1 − UTC, s	X_p/a arc second	Y_p/a arc second
B 4/4/72	−0.356	−0.192	+0.185
C 8/16/72	+0.244	+0.102	+0.433
D 10/14/72	+0.068	+0.164	+0.315
E 10/18/72	+0.055	+0.167	+0.306

Table 4. Goldstone baseline[a] measurements

Experiment	X-component, m	Y-component, m	Z-component, m	Total length, m
A (1/29/71)	−3178.40 ± 0.20	10636.9 ± 0.30	Not measured	–
B (4/4/72)	−3178.57 ± 0.11	10637.08 ± 0.08	11423.34 ± 0.45	15929.33 ± 0.33
C (8/16/72)	−3178.515 ± 0.047	10637.111 ± 0.073	11423.103 ± 0.055	15929.167 ± 0.042
D (10/14/72)	−3178.548 ± 0.025	10637.041 ± 0.045	11423.154 ± 0.034	15929.164 ± 0.021
E (10/18/72)	−3178.568 ± 0.026	10637.132 ± 0.046	11423.115 ± 0.033	15929.196 ± 0.031
Survey 1963-66	−3178.73 ± 0.20	10636.64 ± 0.20	11423.67 ± 0.2	15929.30 ± 0.2

[a]DSS 14–DSS 12.

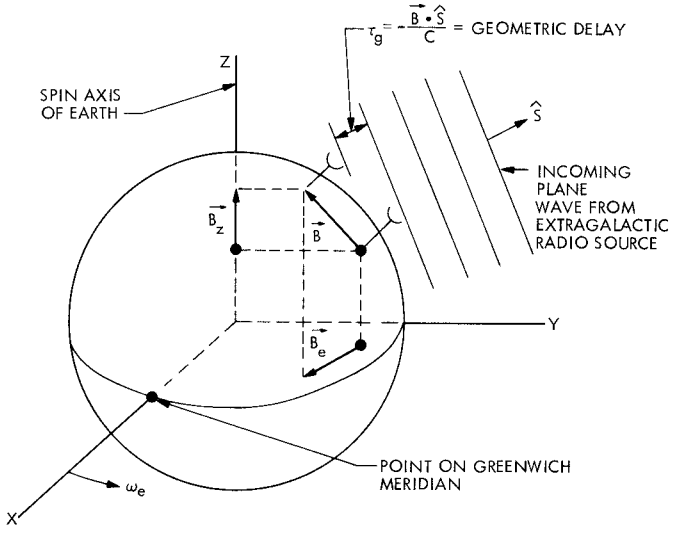

Fig. 1. Geometry of radio interferometry experiments

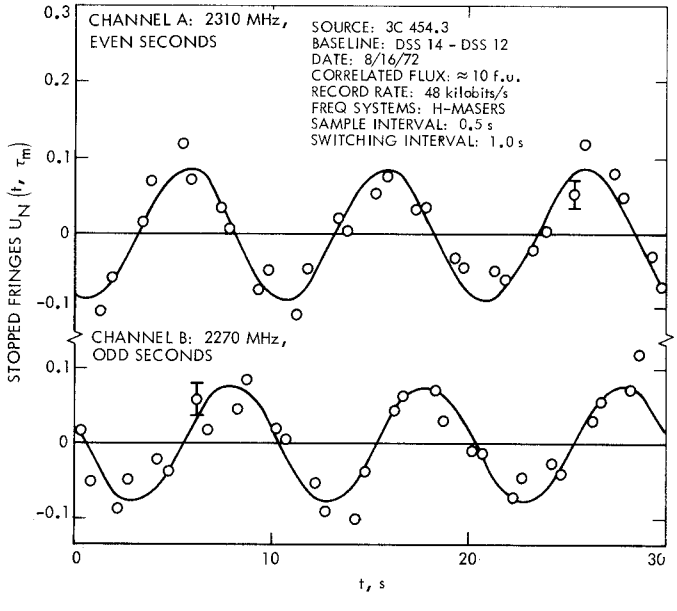

Fig. 2. Stopped fringes for two-channel bandwidth synthesis

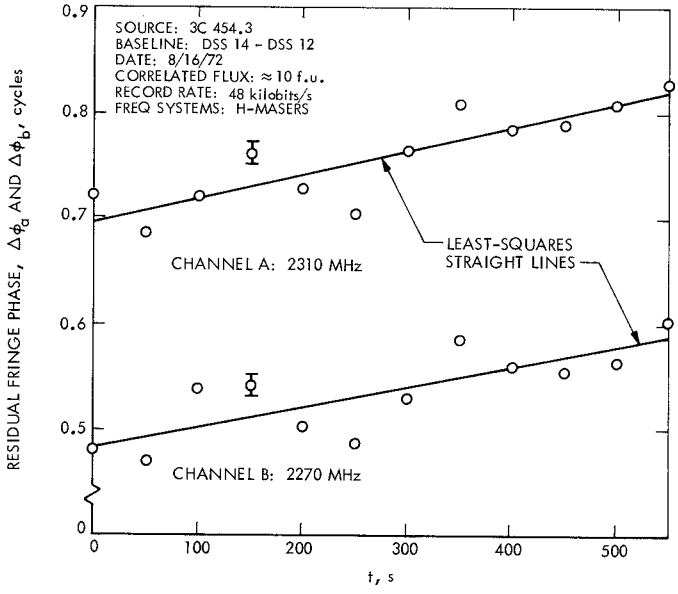

Fig. 3. Fringe phase values for two-channel bandwidth synthesis

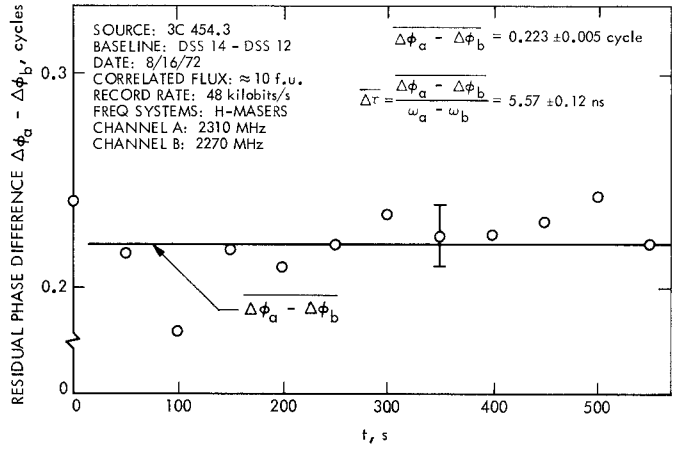

Fig. 4. An example of a delay calculation with two-channel bandwidth synthesis

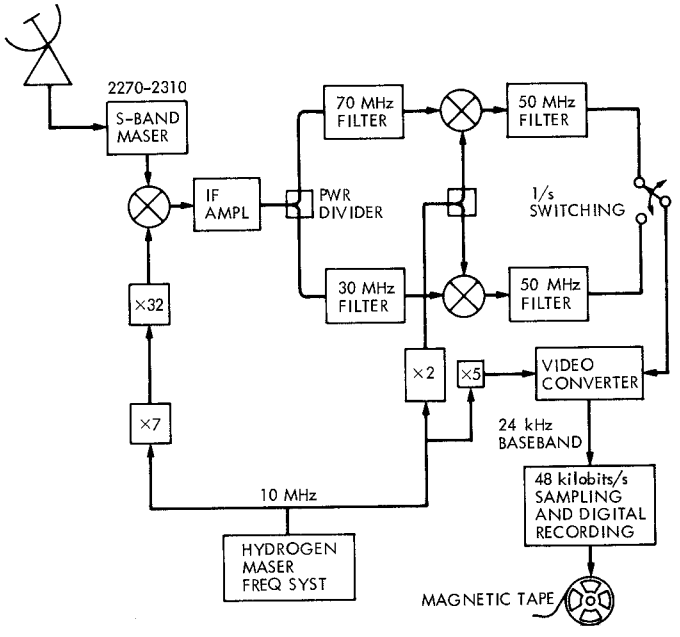

Fig. 5. Deep Space Station configuration for 40-MHz bandwidth synthesis

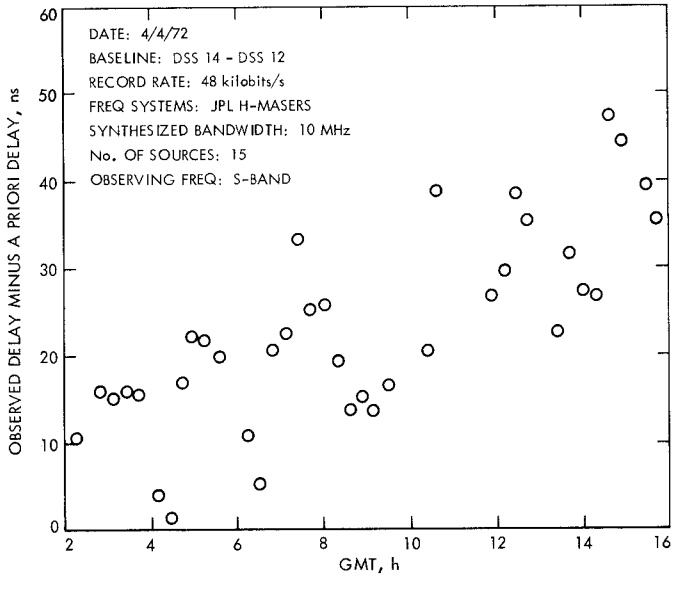

Fig. 6. *A priori* delay residuals for Experiment B

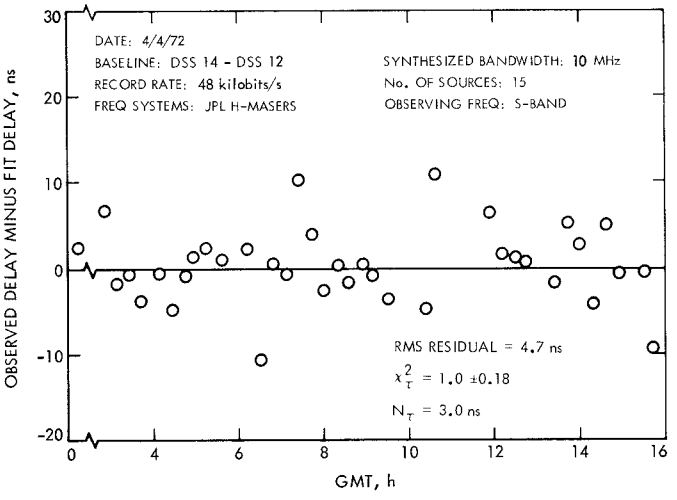

Fig. 7. Fit delay residuals for Experiment B

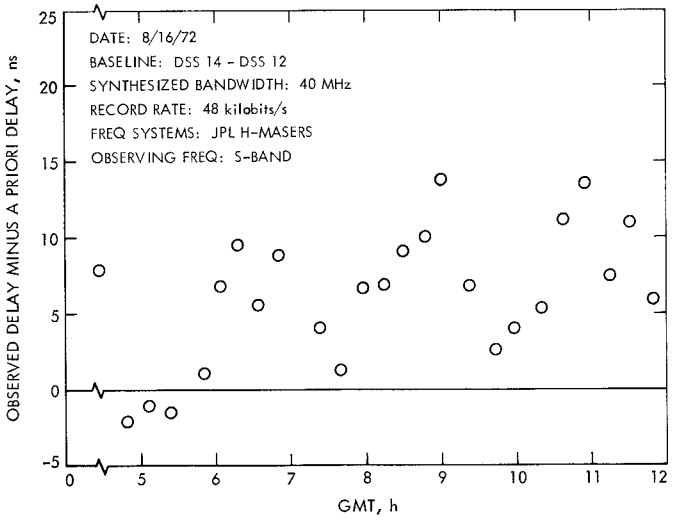

Fig. 8. *A priori* delay residuals for Experiment C

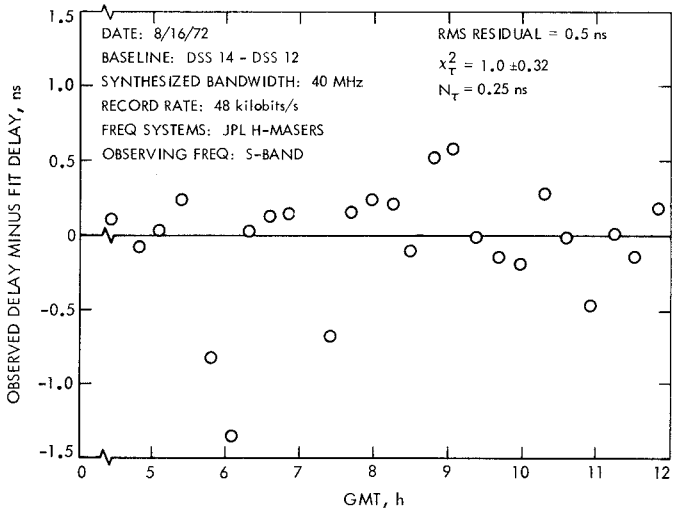

Fig. 9. Fit delay residuals for Experiment C

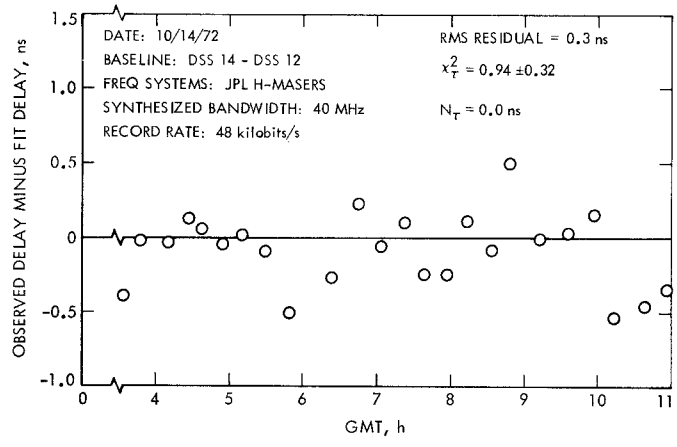

Fig. 10. Fit delay residuals for Experiment D

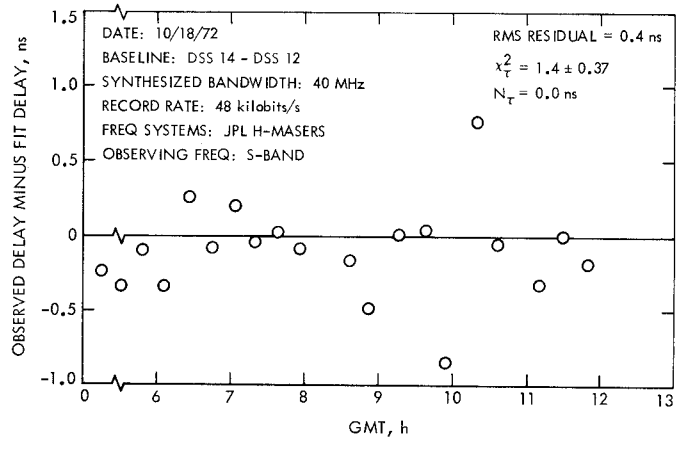

Fig. 11. Fit delay residuals for Experiment E

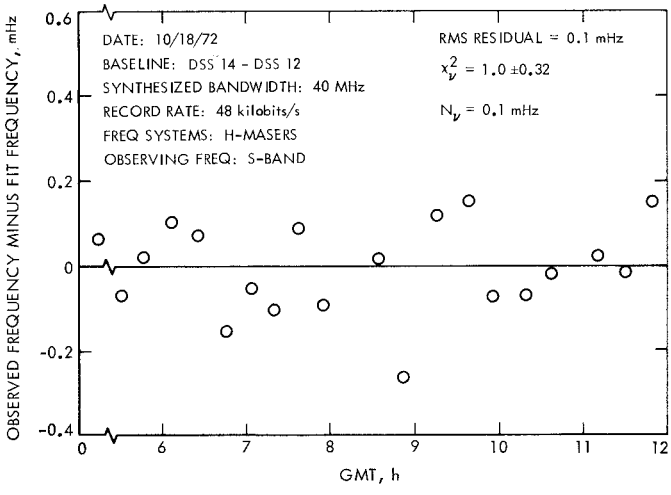

Fig. 12. Fringe frequency residuals for Experiment E

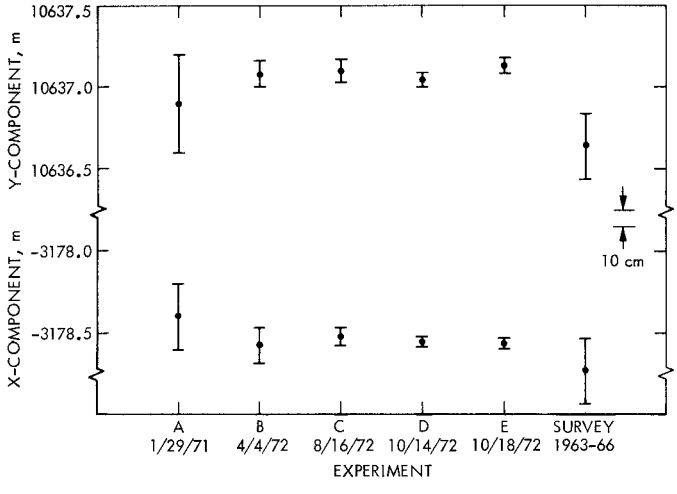

Fig. 13. Goldstone baseline measurements—equatorial projection

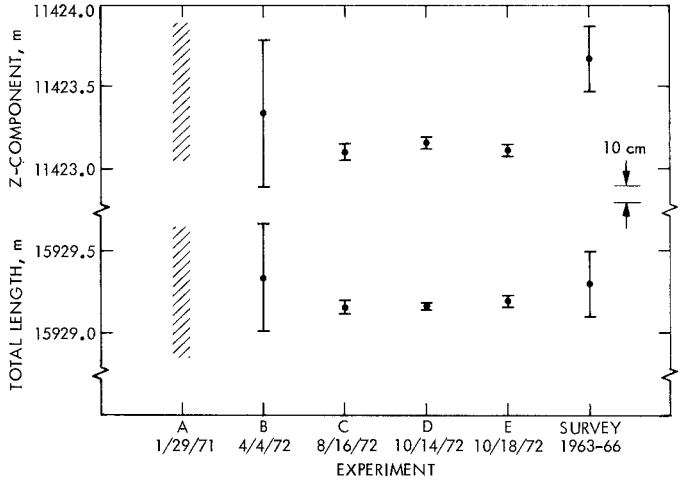

Fig. 14. Goldstone baseline measurements—z component and length